ASME Journal of Engineering for Gas Turbines and Power
Online journal at:
https://asmedigitalcollection.asme.org/gasturbinespower

Dynamic Modeling and Experimental Insights in a 10 kWe Micro Gas Turbine Prototype: Experimental Validation and Testing

Aggelos Gaitanis[1]
Thermal Engineering and Combustion Unit,
University of Mons,
Mons 7000, Belgium
e-mail: angelosevripidis.gaitanis@umons.ac.be

Martin Heylen
MITIS SA,
Liège 4031, Belgium
e-mail: martin.heylen@mitis.be

Sophie Mullender
MITIS SA,
Liège 4031, Belgium
e-mail: sophie.mullender@mitis.be

Ward De Paepe
Thermal Engineering and Combustion Unit,
University of Mons,
Mons 7000, Belgium
e-mail: Ward.DEPAEPE@umons.ac.be

The growing need for decentralized and renewable power generation increases demand for flexible and highly efficient small-scale power units. Microgas turbines (mGTs) are strong candidates for combined heat and power applications in residential, commercial, and industrial sectors, typically delivering below 500 kWe. They can compensate for demand fluctuations in renewable-dominated grids, which can make them ideal for modern energy systems. However, their reliable operation under transient and part-load conditions needs to be assessed, calling for computationally efficient models that enable real-time performance prediction, control, and optimization. In this paper, the development and validation of a dynamic 0D real-time model of a 10 kWe mGT prototype is presented. The MATLAB/Simulink model integrates individual engine components—compressor, turbine, recuperator, combustor, and control system—through refined differential equations. This structure ensures both flexibility and fast computation while capturing key transient dynamics. The 10 kWe prototype, developed by MITIS SA, targets residential energy systems, biomethanization plants, and decentralized power for 5G networks. The system was experimentally validated, as key parameters were measured throughout the cycle under transient and part-load conditions. Key outputs such as shaft speed, turbine inlet temperature, and cycle pressures showed very good agreement with measurements, staying within sensor uncertainty ranges. This validated real-time software provides a modular foundation for future extensions, including humidification, two-stage cycle configurations, and advanced control strategies. [DOI: 10.1115/1.4070464]

Introduction

The decentralization of power generation and growth of renewable energy sources result in the dramatic transformation of energy systems globally. By the end of 2022, solar photovoltaics alone accounted for almost 6% of the world's electricity demand, a substantial improvement from just 3% in 2019 [1]. This trend not only demonstrates that solar energy is one of the electricity sources with the greatest rate of growth in the globe, but it also offers a vision for renewables to become the primary source of new power generation in the next decades. The European climate law, which mandates that european union (EU) emissions must be reduced by at least 55% by 2030, further encourages this shift. EU emissions must be reduced by at least 55% by 2030 according to "Fit for 55" initiative. New legislation is followed by the member states to reach this target by 2050, therefore accelerating the adjustment toward renewable energy [2]. In this context, photovoltaics and wind energy are expected to grow significantly along with electricity demand due to the electrification of various sectors [3]. Where intermittent renewable energy sources become more widespread, reliable backup power systems are gradually becoming more essential. Smaller thermal power plants, like micro gas turbines (mGTs), can play a key role to secure grid stability, particularly in decentralized energy systems, by adapting to fluctuating conditions [4,5].

The continuous transition to decentralized energy systems can profit from the unique advantages that mGT can offer. They are able to offer distributed generation in hybrid energy systems on account of their flexibility, small size, and capacity (100–500 kW_e) [6]. They can operate on a variety of fuels, including biogas, hydrogen, and synthetic alternatives [7]. In addition to complementing renewable energy sources by supplying backup power during periods of low solar or wind generation, they support energy security and control prices. Compared to other combined heat and power technologies, they can offer opportunities for fewer emissions [8] and can pair with waste heat recovery devices to produce combined heat and power.

Turbo Expo: Turbomachinery Technical Conference & Exposition (GT2025) June 16–20, 2025. GT2025.
[1]Corresponding author.
Manuscript received July 15, 2025; final manuscript received July 23, 2025; published online January 30, 2026. Editor: Jerzy T. Sawicki.

Also, mGTs can play a significant role in preserving the grid's stability and dependability because of their low maintenance requirements and high overall (electrical and thermal) efficiency [9]. Such machines quickly ramp up power generation during fluctuations in renewable output to meet the consumer's demand [5].

To ensure effective operation in grids which are dominated by renewable sources of energy, mGTs underwent comprehensive testing under transient and part-load conditions after the development of prototypes. Important performance metrics have been tested and verified against simulation models, which include shaft speed, turbine inlet temperature, and pressure levels. To eliminate operating risks in mGTs connected to large volumes, Ferrari et al. developed a vibration-based control system to show effective surge prevention approaches during transient operations [10]. Banihabib et al. demonstrated the possibility of power generation using sustainable fuels [11] by showcasing the fuel flexibility and minimal NO_x emissions of a 100 kW microturbine running with 100% hydrogen. Based on Liu et al.'s analysis of mGT performance under several intake settings, efficiency is greatly influenced by intake temperature [12]. Wu et al. presented experimental and numerical results to study the off-design overall mGT performance. They demonstrated the high fidelity of simulation predictions under various operating conditions [13]. Caresana et al. evaluated a 100 kW mGT under different thermal loads, reporting an electrical efficiency of 29% and NO_x emissions within regulatory limits [14].

Real-time dynamic modeling plays an important role in predicting as well as optimizing the performance of mGTs in fluctuating power modes. These models are essential in enhancing reliability, efficiency, and flexibility of mGTs, particularly in decentralized systems incorporated with renewable sources. Hosseinalipour et al. created a linear dynamic model of mGTs utilizing state-space formulations to simulate transient behavior. This particular approach simplifies complicated nonlinear equations, making the product computationally effective while keeping high accuracy for off-design conditions [15]. Likewise, Kim et al. created a simulation tool to predict transient responses during load following operations. Their design emphasized the recuperator's thermal inertia in dictating the complete transient response of mGTs [16]. Duan et al. introduced a nonlinear mathematical model, which correctly captures off-design performance of the regenerative mGT cycle and was validated against experimental data under fluctuating load conditions [17]. Xu et al. created a data-driven model to foresee the coupled electrical and thermal outputs of mGT. This tool was effective at capturing system dynamics during transients, providing accuracy of power output in hybrid energy systems [18].

Several articles on dynamic modeling focus on the test bench of T100 mGT. Henke et al. developed a numerical model of mGT dynamics for hybrid energy applications, focusing on interactions between the fuel cells and mGT, validated through high-fidelity simulations [19]. Meanwhile, di Gaeta et al. evaluated transient behavior in a T100 mGT, emphasizing the importance of dynamic simulations in reducing emissions and improving efficiency during off-design conditions [20]. Part of the authors of this paper introduced two significant papers on real-time mGT performance assessment and transient behavior prediction. In the very first paper, they developed an effective real-time mGT performance assessment tool that integrates detailed component modeling methods for turbine and compressor. This particular model gives high-fidelity transient simulations and was validated against experimental data from the VUB T100 test rig, demonstrating under 1% deviation in crucial cycle parameters such as shaft speed and combustor inlet temperature [21]. In the second paper, they proposed a hybrid modeling approach for dynamic mGT simulations. This tool combines data-driven and physical methods to predict the behavior of mGT under transient conditions while decreasing computational efficiency [22].

To increase their adaptability in dynamic energy systems, the transient behavior of mGT operating on different fuels and advanced cycles has been thoroughly investigated. The transient behavior of an OP16 industrial gas turbine running on low-calorific fuels was investigated by Singh et al. [23]. Banihabib et al. developed a dynamic model for a 100 kW mGT operating on blends of methane and hydrogen. This MATLAB Simscape-based model successfully replicated the system's transient behavior and underwent thorough experimental validation, underscoring the significance of fuel flexibility in mGT applications [24]. The transient dynamics of externally fired mGTs were also studied by Traverso et al. utilizing the TRANSEO tool to simulate the behavior of the system during startup and shutdown phases, specifically in biomass-based energy systems [25]. Montero Carrero et al. focused on transient simulations of a microhumid air turbine, showing that water injection improves electrical efficiency and off-design performance. Their model can benefit applications that involve hybrid cycles, where the system must flexibly adjust to varying heat demands [26].

Collectively, these models demonstrate the significance of dynamic simulations in enhancing operation, control, and the design of mGTs. As the energy market continues to shift toward decentralized systems and green energy integration, the capability of mGTs to work efficiently and flexibly in dynamic environments could be vital for ensuring grid stability and reliability.

Despite their fuel flexibility, low emissions, high power density, and minimal maintenance expenses, only a few mGTs are available in the market [9]. Figure 1 depicts the nominal electric power and efficiency output of the mGTs in the market. The majority of the presented mGTs are conventional recuperated Brayton cycles, with the one exception being the Aurelia A400 [27], which is a two-stage intercooled and recuperated Brayton cycle. Capstone Turbine [28] is the most successful mGT manufacturer in the market. Capstone produced two models in the market, the C65 and C200S with electrical efficiencies of 28% and 33% respectively [28]. These designs are the only mGTs equipped with annular recuperator. Flex Energy Solutions [29] developed mGT models (GT250S, GT333S) with higher nominal power, but the performance of Capstone 200S could not be exceeded. MITIS SA designed and manufactured a 10 kW_e mGT which is demonstrated in this paper [30]. The nominal power production of the machine is chosen to target the electricity consumption of residential buildings [31]. Also, as it is shown in Fig. 1 (dotted box), the electrical capacity of the engine covers a gap which is left from the current mGTs in the market, as none of the already manufactured engines covers the region of 5–10 kW_e. We can also see that for nominal power lower than 100 kW_e, the electrical efficiency drops below 30% (EnerTwin [32], Bladon MTP40 [33], Capstone C65 [28]) due to lower turbomachinery efficiency [34], increased heat losses [35], and greater internal leakages [36], adversely affecting overall engine performance. Therefore, the MICRO-10 mGT is carefully designed to present an efficiency close to its competitors with a nominal power of a similar

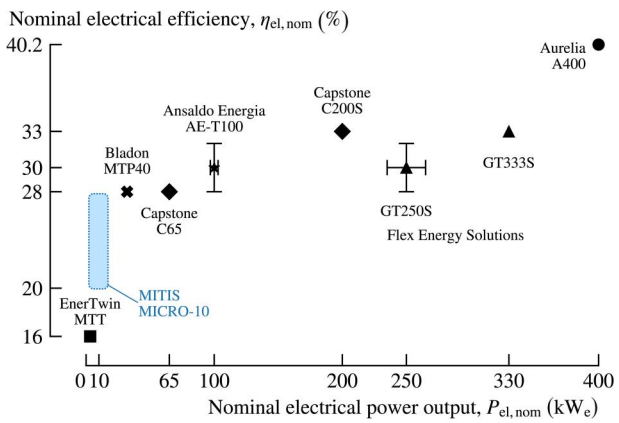

Fig. 1 Microturbine models that are currently in the market. The nominal values refer to the standard or reference values that are provided by the manufacturer at ISO conditions. The MITIS MICRO-10 engine is demonstrated in this paper and produces 10 kW_e.

order of magnitude. However, the operational optimization and control strategy of this engine remains to be assessed with the use of real-time model.

In this paper, we describe the development and verification of a dynamic model for a small-scale decentralized power-generating prototype 10 kW_e mGT. Our goal is to develop a MATLAB/Simulink modular real-time simulation framework that simulates the behavior of key components such as the control systems, compressor, turbine, recuperator, and combustor with precision. We focus on evaluating the mGT's performance under various operating conditions, specifically during part-load and transient scenarios, which can be typical in renewable-heavy power grids. We ensure the model's reliability by comparing its predictions—such as shaft speed, temperatures, and pressures—with experimental data from prototype tests. Ultimately, this research provides a valuable tool for optimizing mGT performance, making it adaptable for use in distributed energy applications where flexibility and efficiency are critical.

Methodology

In the current section, we primarily focus on the methodology adopted to develop, refine, and verify a dynamic model for the MICRO-10 mGT system, along with the representation of the experimental results of the prototype. The methodology combines advanced simulation methods, experimental data analysis, and calibration procedures to ensure the accurate representation of the system's physical actions under both transient and steady-state conditions. Modular modeling strategies in MATLAB/Simulink facilitated the freedom of each component while preserving system interactions. Transient and steady operations have been explored to verify model representation under several conditions. The versatility of the modular architecture empowered targeted independent analysis and refinement. In the end, a calibrated high-fidelity model emerged, quantitatively capturing the MICRO-10 mGT system's intricate dynamics from startup transients to stabilized load variations.

Prototype Characterization. The MICRO-10 mGT system incorporates several innovative features to enhance efficiency and reduce maintenance. The mGT assembly is presented in Fig. 2, and the arrows indicate the direction of the flow stream. The electric motor/generator, turbine, and compressor are installed on a single shaft, eliminating the demand for a gearbox. This particular design decreases lubrication demands and maintenance needs. The rotor achieves speed revolutions up to 100,000 rpm and relies on a permanent magnet synchronous generator to create high-frequency electric power. This power is converted to direct current (DC) and then inverted to 50 Hz alternating current (AC) for standard

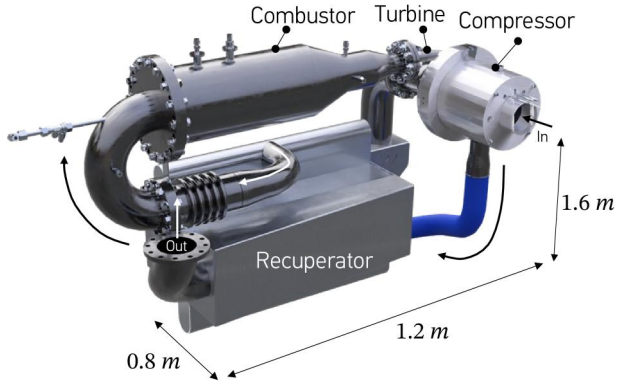

Fig. 2 The outline of MICRO-10 assembly with each component indicated. The arrows show the direction of the flow as well as the inlet and outlet of the cycle. The dimensions of the test bench are included.

applications. Foil bearings are used to minimize friction losses and do not require oil lubrication, simplifying design and maintenance by relying on a thin air cushion for smooth operation [37].

The recuperator plays an important part in recovering waste heat from exhaust gases, drastically upgrading thermal efficiency. MITIS engineers created a novel recuperator architecture, targeting 90% heat recovery with pressure losses under 4% across both fluid paths. This particular refined, cost-conscious invention, drawing inspiration from microchannel heat exchanger technology, applies Computational Fluid Dynamics to optimize heat exchange while reducing component size [38]. Moreover, the combustion chamber employs flameless MILD (Moderate Intense Low oxygen Dilution) combustion technology to lower NO_x and CO emissions. By preheating the reactants above the self-ignition temperature and recirculating combustion products, this particular strategy enhances thermal efficiency while keeping an efficient combustion procedure without an obvious flame front [38,39]. Overall, the MICRO 10 mGT system integrates sophisticated design elements for compactness, efficiency, and low maintenance requirements. Table 1 presents the nominal attributes of the mGT, which are given by the manufacturer and are available online [30]. The targeted electrical efficiency of the cycle is 25% and is mentioned in the MITIS datasheet.

Dynamic Model. The mGT incorporates a speed and fuel controller, which are regulating the produced electrical power and turbine outlet temperature (TOT), respectively. Both controllers are integrated in the dynamic model. In Fig. 3, the front end of the dynamic model is depicted. In the control desk, the user dictates the reference rotational speed (N_{ref}) and reference TOT. The inverter rectifier board (IRB) receives the net torque that is produced by the mGT and the reference speed and gives the actual rotational speed, which is used as input in the mGT. The actual TOT is fed into the fuel controller, which commands the fuel flowrate that is required in the mGT to maintain the reference TOT.

The MICRO-10 module of Fig. 3 is presented in Fig. 4. This mGT model uses similar simulation techniques as those presented in an article by part of the authors [21]. So, several validated techniques of AE-T100 model are applied in the current software [21]. This MATLAB/Simulink model uses inlet and outlet conditions as bus elements. The air flow and fuel flow bus elements include the temperature, static pressure, mass flowrate, composition, and reference values. The constant values are presented in rectangles and the input variables (rotational speed, fuel flowrate) with ellipses. Each component receives as input and gives as output Simulink bus elements that are presented with three-line arrows. Single variables are shown with single-line arrows. The module ***Component matching*** connects compressor's and turbine's operating characteristics. Thus, the outlet pressure of the turbine is calculated from the ambient conditions and the pressure losses and is given as an input to the turbine. Also, the air mass flowrate which is calculated in the turbine, is given to the bus element ***air in***. Initial values are required for the variables of ***point 5′***, the outlet conditions of ***Component matching*** and wherever a differential equation is utilized.

Thermodynamic Calculation. Molar specific enthalpy, entropy, and constant pressure specific heat are assessed using NASA correlations [40], which are a function of temperature. The working fluids used within the model are mixtures of pure gases. The

Table 1 The nominal specifications of MICRO-10 given by the manufacturer

Electric power, $P_{el,nom}$	10 kW_e
Target electrical efficiency, $\eta_{el,nom}$	25%
Rotational speed	100 krpm
Exhaust mass flow rate	160 g/s

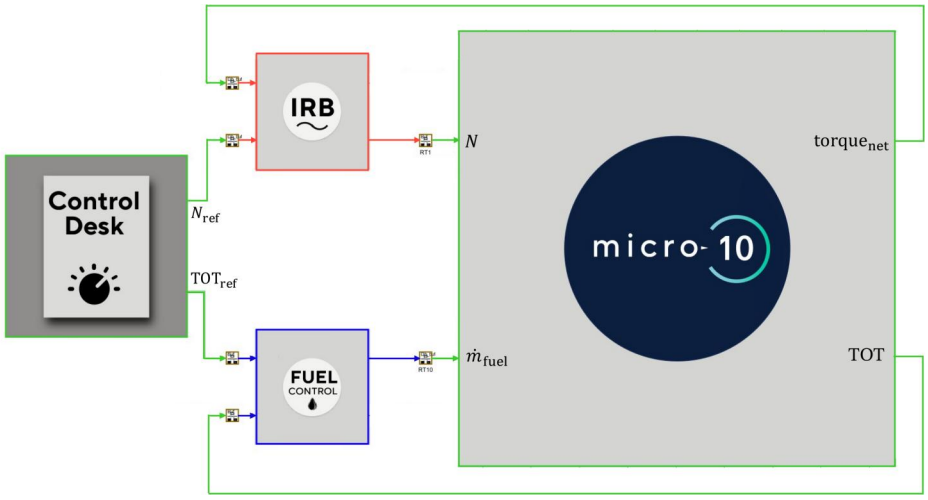

Fig. 3 Dynamic model front end framework. The user gives signal for the reference speed and TOT and the IRB along with the fuel controller gives the required rotational speed and fuel flowrate.

thermodynamic properties (h, c_p, s) are obtained using the molar fraction of each species x_i and their respective molar weight mw_i:

$$h = \sum_i \frac{h_{i,\text{molar}} x_i}{mw_i} \tag{1}$$

$$c_p = \sum_i \frac{c_{p,i,\text{molar}} x_i}{mw_i} \tag{2}$$

$$s = \sum_i \frac{s_{i,\text{molar}} x_i}{mw_i} \tag{3}$$

Compressor. The performance conditions of the compressor and turbine are determined without considering the influence of fluid inertia within the control volume, due to the high flow velocity and small control volume [41]. With this simplification, the conservation equations for mass and energy are applied in their steady-state form, enabling the calculation of the mass flowrate using quasi-steady equations at each time-step.

The compressor pressure ratio $(\pi = p_{\text{out}}/p_{\text{in}})$ and isentropic efficiency (η_{is}) are derived from the compressor map of Fig. 5, which depend on the rotational speed (N) and beta variable (β). The relationship is expressed as follows:

$$(\pi, \eta_{\text{is}}) = f_{c,\text{map}}\left(\beta, \frac{N}{\sqrt{T_{\text{in}}/T_{\text{ref}}}}\right) \tag{4}$$

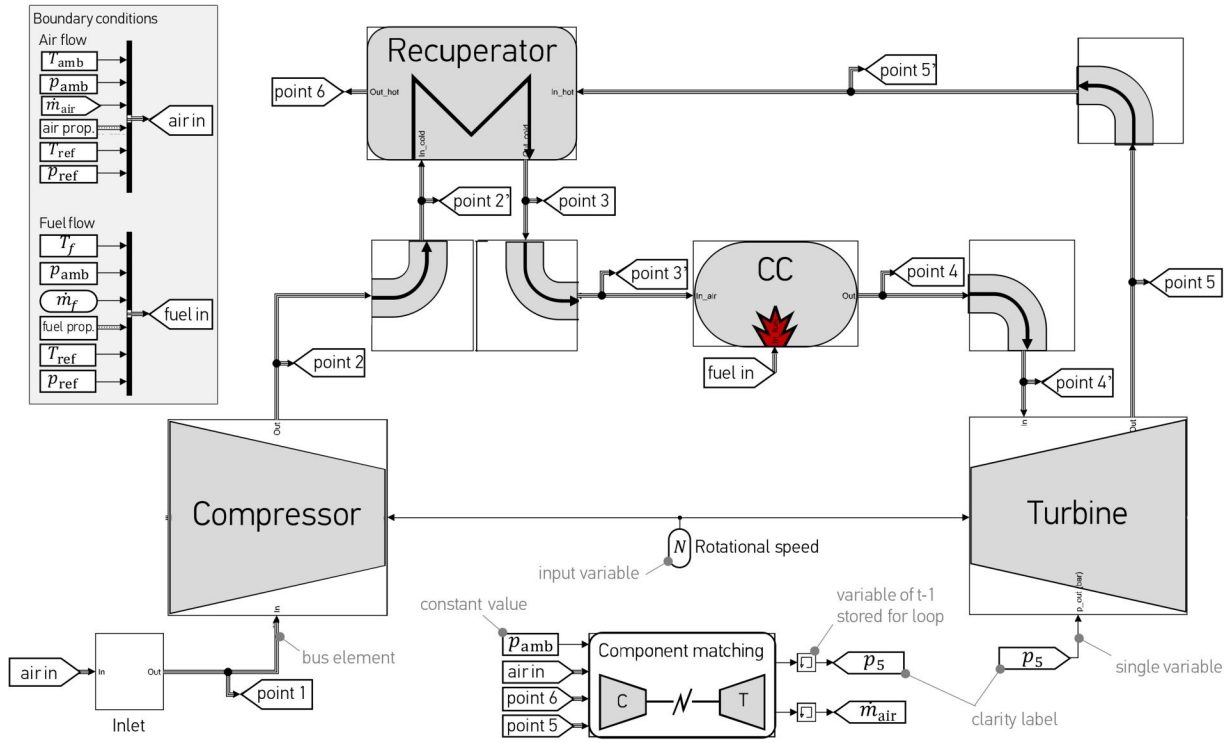

Fig. 4 Detailed model of MICRO-10 in MATLAB/Simulink, presenting the inputs and outputs at each component the type of performance values and the boundary conditions

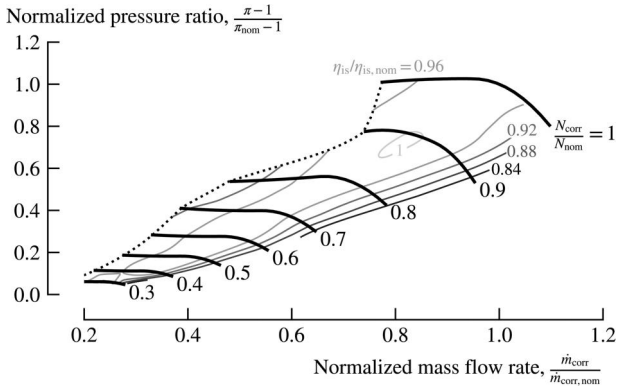

Fig. 5 Normalized compressor performance map depicts the relationship between pressure ratio, mass flowrate, rotational speed and isentropic efficiency. The contour of efficiency lines is generated with cubic interpolation.

where T_{in} and T_{ref} are the inlet and reference temperature, respectively. The reference pressure and temperature are respectively 101,325 Pa and 15 °C. The compressor map is derived from computational fluid dynamics (CFD) analysis by the R&D department of MITIS SA. Moreover, it is presented with normalized values based on the nominal conditions of the cycle.

The compressor outlet temperature (T_{out}) is determined assuming that the working fluid behaves as a perfect gas [21]. Therefore, the isentropic relation is used to calculate the isentropic outlet temperature ($T_{is,out}$) as follows:

$$T_{is,out} = T_{in}\pi^{\frac{\kappa-1}{\kappa}} \tag{5}$$

where κ is the specific heat capacity ratio and is defined as

$$\kappa = \frac{\overline{c_p}(T_{in}, T_{ss,out})}{\overline{c_v}(T_{in}, T_{ss,out})} \tag{6}$$

$\bar{c_p}$ and $\bar{c_v}$ are the average specific heat capacities and $T_{ss,out}$ is the steady-state outlet temperature, which is calculated using the isentropic efficiency ($\eta_{c,is}$) equation applying the specific enthalpy of the states, leading to the following expression:

$$h_{ss,out} = h_{in} + \frac{h_{is,out} - h_{in}}{\eta_{c,is}} \tag{7}$$

The calculated $T_{ss,out}$ is affected during transient conditions due to the thermal capacitance of the component, and also by the heat which is exchanged with the turbine through thermal conduction. By applying energy conservation to this virtual casing [21], the time-dependent outlet temperature is expressed as

$$m_c c_c \frac{dT_{out}}{dt} = \dot{m}(h_{ss,out} - h_{out}) + \dot{Q}_{t-c} \tag{8}$$

where product $m_c c_c$ represents the mass times specific heat capacity of the virtual casing and is calibrated using the inlet parameters of the component from experimental data of the test bench, and simulating the component alone. $\dot{Q}_{t-c}$ is the heat added to the compressor from the turbine, and is calculated from experiments by measuring the temperatures at different parts of the turbomachinery. Then, with conduction analysis of the whole assembly, we ascertain numerically what is the flow of heat from the turbine to the compressor. The pressure ratio and isentropic efficiency are not corrected due to this heat transfer.

Turbine. Similar modeling techniques as in the compressor are applied in the turbine component. The pressure ratio ($\pi = p_{in}/p_{out}$) is calculated knowing the pressure ratio of the compressor and the pressure losses in the combustion chamber and recuperator's hot and cold side. From the pressure ratio, the turbine's beta value is calculated using the turbine performance map shown in Fig. 6. The turbine map is simulated by CFD analysis from the R&D department of MITIS SA. In the next step, the corrected mass flowrate and isentropic efficiency are found using the beta value and corrected rotational speed:

$$\left(\frac{\dot{m}\sqrt{T_{in}/T_{ref}}}{p_{in}/p_{ref}}, \eta_{is}\right) = f_{t,map}\left(\beta, \frac{N}{\sqrt{T_{in}/T_{ref}}}\right) \tag{9}$$

The isentropic outlet temperature is calculated using the same Eqs. (5) and (6) as in the compressor component. Thus, the steady-state outlet temperature is found from the following relation:

$$h_{ss,out} = h_{in} - (h_{in} - h_{is,out})\eta_{t,is} \tag{10}$$

As with the compressor, the outlet temperature is affected by the inertia of the virtual casing the heat losses of this component:

$$m_t c_t \frac{dT_{out}}{dt} = \dot{m}(h_{ss,out} - h_{out}) - \dot{Q}_{t,loss}, \tag{11}$$

where $m_t c_t$ is calibrated as in the compressor component and $\dot{Q}_{t,loss}$ is calculated from experiments. The heat flow parameter is specific to this mGT, as it results from insufficient insulation and temperature gradients within the turbomachinery components.

Recuperator. A standard approach to determine outlet temperatures for the cold (c) and hot (h) streams utilizes a quasi-steady-state assumption for both streams [17,21]. Consequently, the outlet temperatures are expressed as follows:

$$T_{c,out} = \frac{(\dot{m}_c \overline{c_{p,c}} - UA/2)T_{c,in} + UAT_w}{UA/2 + \dot{m}_c \overline{c_{p,c}}} \tag{12}$$

$$T_{h,out} = \frac{(\dot{m}_h \overline{c_{p,h}} - UA/2)T_{h,in} + UAT_w}{UA/2 + \dot{m}_h \overline{c_{p,h}}} \tag{13}$$

where $\bar{c_p}$ in both streams is the average heat capacity between the inlet and outlet flows. UA is the product of the heat transfer coefficient and the heat exchanged surface, which is calibrated to match the heat exchanger effectiveness that is measured in experiments. T_w is the wall temperature from the previous time-step of the simulation. The outlet temperature calculation is iterated until the average heat capacities converge to specific values. This method allows us to avoid modeling a 1-D recuperator component.

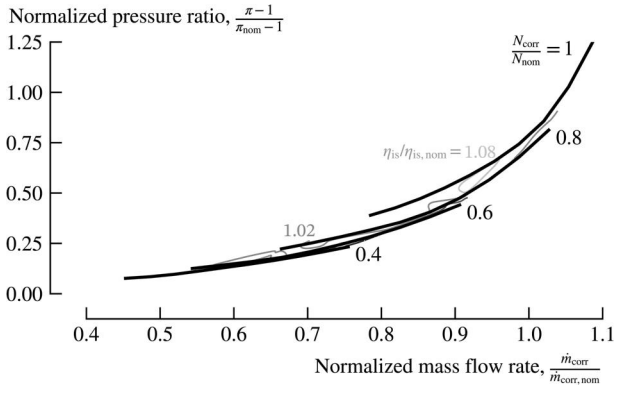

Fig. 6 The turbine map shows the normalized performance parameters of the turbine. The contour of efficiency lines is generated with cubic interpolation.

The hot and cold heat that is transferred across the recuperator is calculated by the following equations:

$$\dot{Q}_c = \dot{m}_c \overline{c_{p,c}}(T_{c,out} - T_{c,in}) \tag{14}$$

$$\dot{Q}_h = \dot{m}_h \overline{c_{p,h}}(T_{h,in} - T_{h,out}) \tag{15}$$

The energy conservation equation is applied to the wall, as demonstrated below:

$$m_{rec} c_{rec} \frac{dT_w}{dt} = \dot{Q}_h - \dot{Q}_c \tag{16}$$

where $m_{rec}c_{rec}$ are the mass and heat capacitance of the recuperator wall, respectively, and their product is calibrated from experimental results. The integration of the differential equations determines the wall temperature (T_w) in the next time-step. The recuperator is assumed to be adiabatic, as it is insulated with 10 cm of glass wool with thermal conductivity of $K = 0.5$ and with 10 cm of compressed wood insulation ($K = 0.19$).

The outlet pressure of the hot and cold streams is calculated, knowing the pressure drop from the experimental results as follows:

$$p_{out} = p_{in} + f(\dot{m}) \tag{17}$$

where $f(\dot{m})$ is a function of the mass flowrate of the cold or hot side. This function is a linear equation for the cold stream and a 2nd-degree polynomial equation for the hot stream.

Combustion Chamber. Although an application of kinetic models for the combustion of natural gas can yield higher accuracy, their limited impact on improving results is often overshadowed by the increased complexity they introduce [42]. Furthermore, factors such as residence time and temperature distributions are difficult to assess in dynamic models, ultimately restricting the accuracy achievable with these kinetic schemes. Also, the majority of the bibliography in dynamic modeling of mGT avoids kinetic models for the combustion chamber [5].

Therefore, a quasi-steady-state, single-step model is adopted, assuming the complete combustion of a homogeneous air/fuel mixture. This model describes the oxidation of fuel in air (comprising only N_2, O_2, and Ar) as follows:

$$kC_xH_y + mO_2 + pN_2 + qH_2O + rAr \Rightarrow$$
$$kxCO_2 + \left(\frac{ky}{2} + q\right)H_2O + \left(m - n - \frac{ky}{4}\right)O_2 + pN_2 + rAr \tag{18}$$

where k, m, p, q, r are the moles of each molecule that takes part in the combustion. C_xH_y depicts the hydrocarbons in the air/fuel mixture. Nonhydrocarbon fuels such as N_2 and Ar are considered nonreactive and are treated as chemically inert species. This model can be utilized to evaluate the composition of flue gases resulting from the oxidation of fuels primarily consisting of alkanes.

The energy conservation equation is constructed knowing the heat released and the inlet and outlet conditions of this component as

$$m_{cc} c_{cc} \frac{dT_{out}}{dt} = \dot{m}_{in} h_{in} + \dot{m}_f (h_f + LHV\eta_{cc}) - \dot{m}_{out} h_{out} \tag{19}$$

where η_{cc} is the combustion efficiency of a mild burner, which typically is higher than 99% [43]. For the purposes of this study, we assumed the value of 99.5% [43]. h_{out} is the outlet specific enthalpy that is calculated from the outlet temperature of the previous time-step. Lower heating value (LHV) is the lower heating value of the fuel with a composition (mole fractions) of CH_4: 90%, C_2H_6: 9.3%, CO_2: 0.7%, $\dot{m}_f$ and h_f is the mass flowrate and specific enthalpy of the fuel, respectively. $\dot{m}_f$ is established by the fuel controller and h_f is calculated by the boundary condition T_f, which is 30 °C for the validation. The mass inertia ($m_{cc}c_{cc}$) is calibrated based on experimental data, following the same approach used for other components. Moreover, the pressure drop of the combustor is determined from experiments.

Generator. The rotational speed of the shaft is determined by a differential equation that accounts for the power generated and consumed during dynamic operation. This energy balance is represented as:

$$I\omega \frac{d\omega}{dt} = P_t - P_c - P_b - P_{pe} - P_{el} \tag{20}$$

where ω is the angular velocity of the shaft in rad/s, and I represents the moment of inertia. The terms in the equation include P_t, the power generated by the turbine; P_c, the power required by the compressor; P_b, the power lost due to the bearings; P_{pe}, the power consumed by the electronics; and P_{el}, the power output of the generator, which is regulated by the control system.

The bearing losses are determined from the experimental results at the nominal point for the current study. Furthermore, the generator is modeled with an electronic efficiency of 99%, while the power electronics are assumed to operate with a conversion efficiency of 95% [21].

Pipes. The outlet pressure in the pipes connecting the components is calculated from a correlation that is made from experimental data of the MICRO-10 test rig as

$$p_{out} = p_{in} - (a \cdot \dot{m}_{corr}^2 + b \cdot \dot{m}_{corr}) p_{in} \tag{21}$$

where a,b are the parameters of the correlation and $\dot{m}_{corr}$ is the corrected mass flowrate of the pipe and is $\dot{m}_{corr} = \dot{m}\sqrt{T_{in}/T_{ref}}/(p_{in}/p_{ref})$. The pressure difference (Δp) between the inlet and outlet of the pipes is measured to be between 63 and 1180 Pa. Also, the pipe between the turbine and recuperator presents the highest losses at 1180 Pa.

Control System. As it is shown in Fig. 3 the control system of the mGT and of dynamic model is divided into two parts, the speed controller which is represented by the IRB, and the fuel controller.

One crucial part which is modeled in Simulink to replicate the operation and power output control logic is the IRB. In motor function, it performs as an inverter; in generator function, it acts as a rectifier. In motor function, the IRB powers the compressor to keep the combustion chamber's pressure in the essential level. The component transitions to generator setting, therefore the IRB is able to recover energy and re-inject it into the DC bus whenever the power recovered from the turbine surpasses the input of the engine. A three-phase bridge made of silicon carbide transistors is utilized to replicate the hardware. Cable resistance for wiring losses, motor winding inductance and resistance, back electromotive force (EMF) voltage to imitate electromotive force, then ground resistance for leakage currents are contained in every stage. Current and voltage sensors are employed in each stage to ensure safety and also give feedback for motor system control. The control system calculates duty cycles dependent on magnetic field and speed measurements angles, working on two levels: high frequency torque control at 28 kHz for controlling engine torque and also low-frequency speed control at 100 Hz for regulating turbospeed. The model gives as outputs the duty cycles for every stage along with the phase advance direction, that is applied to evaluate alignment and torque of the electric and magnetic fields. All in all, the Simulink design can serve as an essential tool for simulating the IRB's hardware control algorithms, enabling comprehensive performance analysis for effective operation in motor and also generator modes.

The fuel control system incorporates a TOT control loop that maintains a consistent TOT throughout the simulation. A proportional integral controller is applied, and the gains K_p, K_i are calibrated to minimize the steady-state error and the settling time.

More information regarding the IRB and fuel controller is confidential.

Instrumentation. The test bench located at MITIS headquarters features the MICRO-10 microgas turbine, designed for residential power applications. The system has a nominal electric power output of 10 kW_e and it operates with a nominal rotational speed of 100 krpm. Table 2 provides details of the sensors used in the MICRO-10 test bench. Measurements were recorded at a frequency of 10 Hz. For temperature measurements, type K thermocouples were employed. Most temperature sensors are of Class 2, with an accuracy of ±2.5 °C or 0.75% of the measured temperature, while the TOT sensor is Class 1, with an accuracy of ±1.5 °C or 0.4% of the measured temperature. Pressure sensors have an accuracy of 0.2% which is linked with the full-scale values, also there is minimal thermal error due to the use of long capillaries. The fuel flow controller measures with an error of ±1.5% (1% of the reading +0.5% of the full scale) and is calibrated for a natural gas flow at nominal conditions. The mass flowrate of the air flow is measured with hot-film air mass meter, type HFM 5 by Bosch, with a maximum error of ±3%.

Regarding the temperature measurements, we use two thermocouples at the entrance and exit of the combustion chamber and a double thermocouple for the turbine outlet temperature, all positioned at the midpoint of the pipe diameter for a representative temperature measurement. While pipe diameters vary by component, we ensure that the cycle mass flow keeps total pressure and temperature variations low.

Results and Discussion

To validate the accuracy of the developed model, a steady-state analysis was first performed at nominal power by comparing key engine parameters with experimental data from the MICRO-10 test bench. Subsequently, the transient response of the model was also validated and evaluated against experimental data recorded during dynamic operation of the MICRO-10 system.

The presence of heat added in the compressor and heat that is lost in the turbine influence the isentropic efficiencies of the components. Therefore, this phenomenon generates the necessity to perform an initial sensitivity analysis on the electrical efficiency as the isentropic efficiencies are varied. So as the isentropic efficiency of the compressor decreases by 1%, 5%, and 10%, we observed that the electrical efficiency is reduced by 0.36%, 1.92%, and 4.15% points, respectively. Moreover, as the turbine isentropic efficiency drops by 1%, 5%, and 10%, the electrical efficiency is deteriorating by 0.58%, 3.01%, and 6.24%, consequently. These results showcase the stronger effect of the turbine's efficiency than the compressor's in the performance of the cycle. Also, it is shown that the effective management of the heat losses will directly increase the cycle's efficiency by several percentage points. For a detailed uncertainty quantification and robust optimization of an mGT cycle, we recommend the reader to refer to a study written by part of the authors of this paper [44].

In the validation subsections, the relative error compared to experiments and also the depiction of parameters is presented as follows:

Table 2 Details and precision of the measured parameters

Parameter	Location	Accuracy
Temperature	Inlet, outlet of components	±0.75%
Temperature	Turbine outlet (TOT)	±0.4%
Pressure	Inlet, outlet of components	±0.2%
Shaft speed, N	Controller	±0.5%
Mass flow rate, $\dot{m}_f$	Controller	±1.5%
Mass flow rate, $\dot{m}_a$	Inlet	±3%

$$e_x = \frac{|x_{exp} - x|}{x_{exp}} 100\%, \quad x_{norm} = \frac{x}{x_{nom,exp}} \tag{22}$$

where x is a performance parameter, e is the relative error and x_{exp} is the measured performance parameter during experiment. Therefore, the presented performance parameters of this study are normalized to respect the confidentiality of the manufactured prototype. At last, transient results are presented in this chapter during a rotational speed step response to confirm the model's ability to simulate part-load changes.

Steady-State Validation. Figure 7 illustrates the relative error of Eq. (22) for various performance parameters at the nominal operation MICRO-10 mGT. The comparison between the experimental and simulated data shows excellent agreement in temperatures across all the measured stages of the cycle. The deviations of temperatures observed are close or fall within the uncertainty margins of the measurement sensors, reinforcing the accuracy of the model. Three pressure values present a relative error higher than 2% with the highest value to be shown at the compressor outlet. This error is associated with the behavior of the compressor, and it is passed on to the other components. The compressor of the test bench receives a heat flow from the turbine, which deteriorates its performance. This heat diverges the compression process further away from the ideal isentropic. As a result, the outlet temperature is increasing and the pressure ratio is decreasing. However, this error could be calibrated in the future, including a more detailed differential equation and calculating the real process rather than an isentropic.

The rotational speed of the shaft shows the lowest error, confirming the accurate modeling of the IRB component. Moreover, the air mass flowrate presents a deviation from the experiment less than the accuracy of the air flowmeter ($\leq 3\%$). This result certifies that the pressure ratio of the turbine along with the turbine map accurately predict the gas mass flowrate of the cycle.

These results demonstrate the model's ability to replicate the steady-state behavior of the mGT accurately. Such fidelity is essential for establishing a reliable baseline for further exploration of transient dynamics. The agreement also indicates that the assumptions made in the model, such as neglecting minor heat losses and assuming idealized component behavior, are reasonable

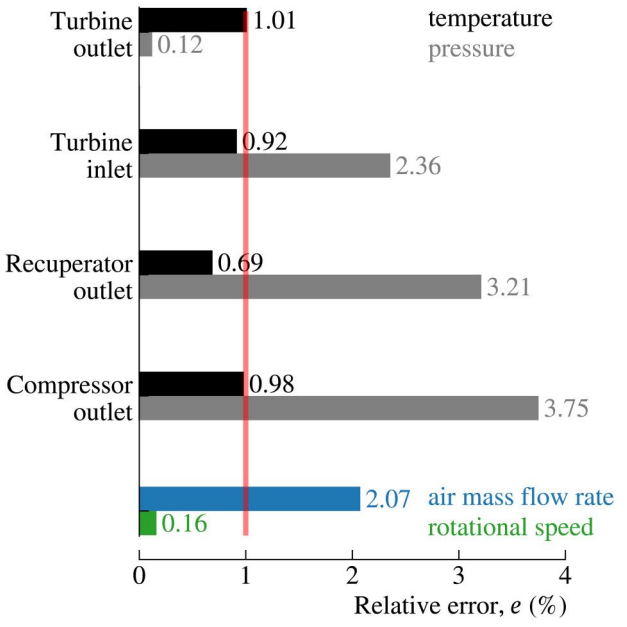

Fig. 7 The relative error from experiments of significant performance parameters is not more than 4%. Temperature and shaft speed present high accuracy.

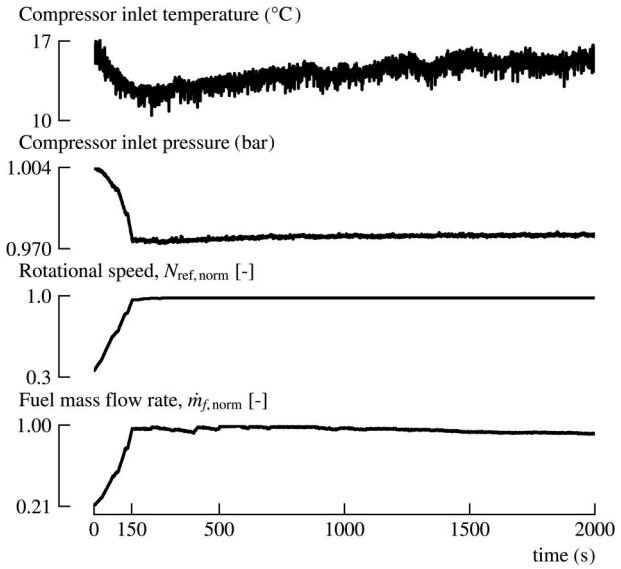

Fig. 8 Input parameters for the transient validation of the model. The fuel mass flowrate and the reference shaft speed are the input control parameters. The boundary conditions are applied with the compressor inlet temperature and pressure.

under steady-state conditions. This validation ensures the robustness of the model and highlights its potential for optimization and operational analysis.

Dynamic Validation. For the dynamic validation, an experimental test in which the recuperator is already hot is utilized (typically called a hot start). This study provides useful information regarding the performance of the model while specific initial conditions are applied.

Figure 8 presents the input parameters, including rotational speed and fuel flowrate, used to evaluate the dynamic response of the system. Compressor inlet temperature and pressure are the boundary conditions of the simulation. As the fuel flowrate is increasing (0–150 s) from 21% to 100% and shaft speed from 30% to 100%, the air mass flowrate is increasing to maintain a lambda value in the combustion of 1.3. This acceleration behavior elevates the pressure losses in the compressor inlet and decreases the temperature within this time range.

The reference rotational speed and the fuel flowrate are intentionally fed into the system to emulate a restart of the mGT while it did not have time to cool down from its previous run. The controlled nature of these variations allows us to systematically assess the model's transient behavior, ensuring it is responsive to realistic operational scenarios.

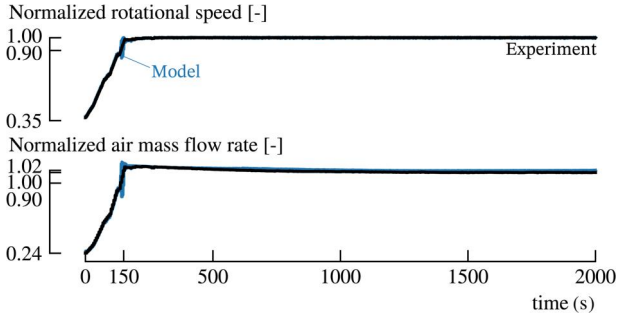

Fig. 9 Rotational speed and air mass flowrate simulation results show high fidelity with experimental data during an acceleration of the mGT

Figures 9–11 show collectively the dynamic validation results, by comparing the outputs of the model with the measured values from experimental test. In Fig. 9, we depict the device's rotational speed and air mass flowrate during transient operation. The model effectively predicts the pattern of acceleration, displaying outstanding agreement with the experimental data. The IRB presents shaft speed error during the transient under 1%. Furthermore, the turbine map properly calculates the gas mass flowrate, with an error less than 5% in the entire transient test. This particular result validates the implemented speed control approach and also the model's handling of rotational dynamics under transient conditions. Additionally, it underscores the model's capacity to conform to sudden changes in running modes, that is vital for keeping balance in decentralized power grids.

In Fig. 10 we present the temperature transients at four different positions in the cycle. The compressor outlet temperature presents a maximum error of 6.3% at 163 s. However, this value is quickly diminished as the average remains at 1%. The turbine outlet temperature demonstrates the lowest average error of 0.86%. Recuperator outlet temperature follows with an error of 0.93% and turbine inlet shows 0.95%. Therefore, these results exhibit the model's ability to accurately track thermal transients during rapid changes with the effective calibration of thermal inertias and heat exchange dynamics in the differential equations within the model's system. Minor discrepancies observed are likely due to unmodeled factors, such as localized heat losses, which could be modeled in the future as they are outside the scope of this article.

The pressure profiles for the acceleration of the mGT are shown in Fig. 11. As it is confirmed with the steady-state validation, the turbine outlet pressure presents the lowest error at nominal conditions due to the accurate modeling of the pressure losses of the cycle. At low rpm the error increases but remains less than 1%. In general, the trend of pressure increase during the acceleration and nominal conditions is captured adequately regardless of the error that is shown in the compressor outlet pressure, which is explained in the "Steady-state validation" subsection.

Dynamic Results. We examined the transient response of the mGT model by performing load step changes in rotational speed, as revealed in the upper diagram of Fig. 12 with the N_{ref} action. The normalized rotational speed (N_{norm}) exhibits discrete steps over time that last several minutes, reflecting the applied reference values of N_{ref}. We can observe that, the model effectively tracks these changes

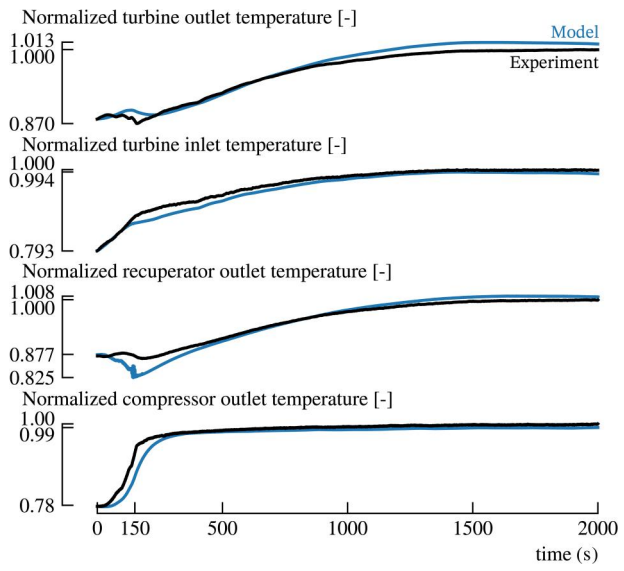

Fig. 10 Temperature profiles during an acceleration of the mGT at four different positions. The average error remains below 1% in the modeled temperatures.

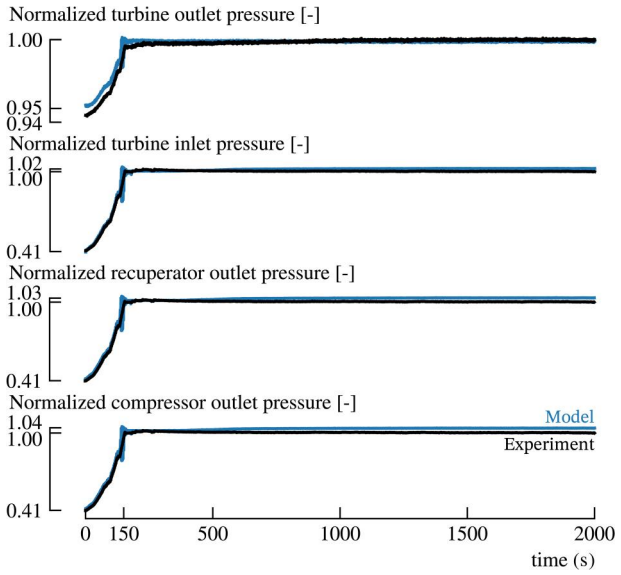

Fig. 11 Pressure profiles during the acceleration of the mGT. The turbine outlet pressure exhibits minimal error at nominal conditions due to accurate modeling of pressure losses, with errors at low rpm increasing but remaining below 1%.

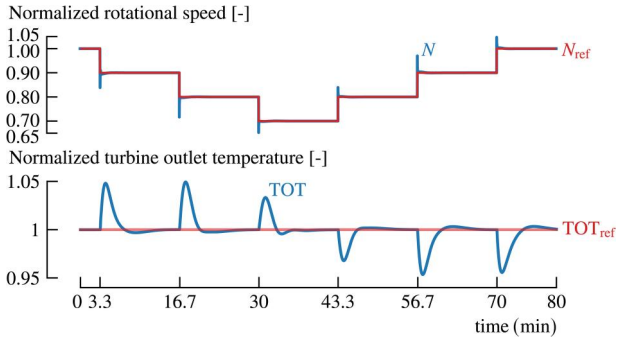

Fig. 12 Normalized rotational speed and TOT during transient load step changes of the mGT model, highlighting the fuel control system's and IRB's effectiveness in maintaining stability around the reference values

with fast response, demonstrating the robustness of the speed management system which is implemented by MITIS. The small overshoot that is shown between N and N_{ref} highlights the effective implementation of the IRB into Simulink as well as the accurate modeling of the system's dynamics and inertia (I).

The bottom segment of Fig. 12 illustrates the normalized TOT compared with its reference value (TOT_{ref}). Throughout the step changes in rotational speed, the TOT exhibits small oscillations, reflecting the transient adjustment of the gas flowrate to complement the required operating conditions. At negative shaft speed steps, the air/fuel ratio decreases instantaneously, increasing the TOT. At positive steps the air/fuel ratio increases respectively which reduces the TOT. The fuel control system successfully minimizes the overshoot and stabilizes the TOT within a narrowband around TOT_{ref}. The close agreement between the measured TOT and TOT_{ref} indicates the fidelity of the fuel control strategy and the accurate thermal modeling of the system.

Conclusions

In this paper, we presented the development and validation of a dynamic model for a novel 10 kW_e mGT. Also, we demonstrated the first experimental results of the prototype that are utilized for validation purposes. The constructed model aimed to provide a real-time simulation framework to replicate the transient and steady-state behavior of the system. Speed, temperature, and pressure parameters presented minimum error with the measurements, validating the model's dynamic representation. Also, the model's ability to track reference control values while maintaining stability during acceleration highlights its applicability for real-time control. Additionally, we applied transient step responses to further provide results regarding dynamic reliability. Under several step responses, the shaft speed and fuel control systems operate dependably, remaining steady also strongly following with the reference values. By directly replicating experimental results, the code offers a strong framework for analyzing and also optimizing mGT operations under different transient conditions, making sure reliability and adaptability in renewable-dominated power systems.

In future work, a number of improvements and innovations will assist the performance and versatility of this system. Data collected from experiments will be used to fine-tune heat losses and performance map curves, raising model accuracy. A proportional–integral–derivative (PID) controller could be used for the fuel management system, with careful tuning of K_p, K_d, and K_i to minimize overshoot and improve stability. Increasing K_d while moderating K_p and K_i helps achieve a well-balanced response, but an optimization algorithm could also be implemented to dynamically adjust these gains for optimal performance. A humidification tower will also be integrated and tested in UMARC laboratory at University of Mons, transforming it into the microhumid air turbine. This will increase the flexibility and efficiency of the system toward integration to sustainable energy applications.

Acknowledgment

Views and opinions expressed are however those of the author(s) only and do not necessarily reflect those of the European Union or CINEA. Neither the European Union nor the granting authority can be held responsible for them ("Fit4Micro-Clean and efficient micro-CHCP by microturbine based hybrid systems"). This paper reflects only the authors' view and the Research Executive Agency, and the European Commission are not responsible for any use that may be made of the information it contains.

Funding Data

- European Union (Award ID: 101083536; Funder ID: 10.13039/501100000780).

Data Availability Statement

The datasets generated and supporting the findings of this article are obtainable from the corresponding author upon reasonable request.

Nomenclature

Acronyms

CC = combustion chamber
CHP = combined heat and power
IRB = inverter rectifier board
mGT = micro gas turbine
ODE = ordinary differential equation
PI = proportional integral
PMSG = permanent magnet synchronous generator
REC = recuperator
TIT = turbine inlet temperature, °C
TOT = turbine outlet temperature, °C

Roman Symbols

c_p = mass heat capacity, kJ/(kgK)
h = mass specific enthalpy, J/kg

I = moment inertia, kg m^3
k = heat capacity ratio
m = mass, kg
N = rotational speed, rpm
P = power output, kW
p = pressure, Pa
s = mass specific entropy, J/kg/K
T = temperature, °C
t = time, s

Greek Symbol

η = efficiency, %

Subscripts

el = electrical
nom = nominal
norm = normalized
ref = reference

References

[1] International Energy Agency Photovoltaic Power Systems Programme (IEA-PVPS), 2020, "Snapshot 2020," International Energy Agency, Paris, France, accessed Dec. 3, 2023, https://www.iea-pvps.org/
[2] European Council, 2024, "Fit for 55 - The EU's Plan for a Green Transition," European Council, Brussels, Belgium, accessed Apr. 4, 2024, https://www.consilium.europa.eu/en/policies/green-deal/fit-for-55/
[3] International Energy Agency (IEA), 2022, "Energy Transitions Require Innovation in Power System Planning," International Energy Agency, Paris, France, accessed Nov. 12, 2023, https://www.iea.org/articles/energy-transitions-require-innovation-in-power-system-planning
[4] International Energy Agency (IEA), 2022, "World Energy Outlook 2022," International Energy Agency (IEA), Paris, France, Nov. 8, 2024, https://www.iea.org/reports/world-energy-outlook-2022
[5] Hashmi, M. B., Mansouri, M., and Assadi, M., 2023, "Dynamic Performance and Control Strategies of Micro Gas Turbines: State-of-the-Art Review, Methods, and Technologies," Energy Convers. Manage.: X, **18**, p. 100376.
[6] Kolanowski, B. F., 2004, *Guide to Microturbines*, Fairmont Press, Lilburn, GA, New York.
[7] Ismail, M., Moghavvemi, M., and Mahlia, T., 2013, "Current Utilization of Microturbines as a Part of a Hybrid System in Distributed Generation Technology," Renewable Sustainable Energy Rev., **21**(C), pp. 142–152.
[8] Pilavachi, P. A., 2002, "Mini- and Micro-Turbines for Combined Heat and Power," Journal of," Appl. Therm. Eng., **22**(18), pp. 2003–2014.
[9] Prasad, K., and Jukka, R., 2013, "Generation of Heat and Power From Biogas for Stationary Applications: Boilers, Gas Engines and Turbines, Combined Heat and Power (CHP) Plants and Fuel Cells," *The Biogas Handbook*, Woodhead Publishing, Cambridge, UK, pp. 404–427.
[10] Ferrari, M. L., Silvestri, P., Reggio, F., and Massardo, A. F., 2018, "Surge Prevention for Gas Turbines Connected With Large Volume Size: Experimental Demonstration With a Microturbine," Appl. Energy, **230**, pp. 1057–1064.
[11] Banihabib, R., Lingstädt, T., Wersland, M., Kutne, P., and Assadi, M., 2024, "Development and Testing of a 100 kW Fuel-Flexible Micro Gas Turbine Running on 100% Hydrogen," Int. J. Hydrogen Energy, **49**, pp. 92–111.
[12] Cong, L., Zhijun, S., Yimin, L., Zhongning, Z., and Lina, M., 2024, "Experimental Study on the Performance of Micro Gas Turbines Under Different Intake Environments," Case Stud. Therm. Eng., **58**, p. 104415.
[13] Wu, X., Hu, X., Xiang, X., Lin, S., You, J., and Tian, F., 2023, "An Analysis Approach for Micro Gas Turbine Engine's Performance by Experiment and Numerical Simulation," Case Stud. Therm. Eng., **49**, p. 103305.
[14] Caresana, F., Comodi, G., Pelagalli, L., Renzi, M., and Vagni, S., 2011, "Use of a Test-Bed to Study the Performance of Micro Gas Turbines for Cogeneration Applications," Appl. Therm. Eng., **31**(16), pp. 3552–3558.
[15] Hosseinalipour, S. M., Abdolahi, E., and Razaghi, M., 2013, "Static and Dynamic Mathematical Modeling of a Micro Gas Turbine," J. Mech., **29**(2), pp. 327–335.
[16] Kim, M. J., Kim, J. H., and Kim, T. S., 2016, "Program Development and Simulation of Dynamic Operation of Micro Gas Turbines," Appl. Therm. Eng., **108**, pp. 122–130.
[17] Duan, J., Sun, L., Wang, G., and Wu, F., 2015, "Nonlinear Modeling of Regenerative Cycle Micro Gas Turbine," Energy, **91**, pp. 168–175.
[18] Xu, X., Li, K., Jia, H., Yu, X., Deng, J., and Mu, Y., 2018, "Data-Driven Dynamic Modeling of Coupled Thermal and Electric Outputs of Microturbines," IEEE Trans. Smart Grid, **9**(2), pp. 1387–1396.
[19] Henke, M., Monz, T., and Aigner, M., 2017, "Introduction of a New Numerical Simulation Tool to Analyze Micro Gas Turbine Cycle Dynamics," ASME J. Eng. Gas Turbines Power, **139**(4), p. 042601.
[20] Di Gaeta, A., Reale, F., Chiariello, F., and Massoli, P., 2017, "A Dynamic Model of a 100 kW Micro Gas Turbine Fuelled With Natural Gas and Hydrogen Blends and Its Application in a Hybrid Energy Grid," Energy, **129**, pp. 299–320.
[21] Gaitanis, A., Contino, F., and De Paepe, W., 2023, "Real Time Micro Gas Turbines Performance Assessment Tool: Comprehensive Transient Behavior Prediction With Computationally Effective Techniques," ASME J. Eng. Gas Turbines Power, **145**(3), p. 031006.
[22] Gaitanis, A., Laterre, A., Contino, F., and De Paepe, W., 2022, "Towards Real Time Transient mGT Performance Assessment: Effective Prediction Using Accurate Component Modelling Techniques," J. Global Power Propul. Soc., **6**, pp. 96–105.
[23] Singh, V., Axelsson, L.-U., and Visser, W., 2017, "Transient Performance Analysis of an Industrial Gas Turbine Operating on Low-Calorific Fuels," ASME J. Eng. Gas Turbines Power, **139**(5), p. 051401.
[24] Banihabib, R., and Assadi, M., 2022, "Dynamic Modelling and Simulation of a 100 kW Micro Gas Turbine Running With Blended Methane/Hydrogen Fuel," ASME Paper No. GT2022-81276.
[25] Traverso, A., Massardo, A. F., and Scarpellini, R., 2006, "Externally Fired micro-Gas Turbine: Modelling and Experimental Performance," Appl. Therm. Eng., **26**(16), pp. 1935–1941.
[26] Montero Carrero, M., Ferrari, M. L., De Paepe, W., Parente, A., Bram, S., and Contino, F., 2015, "Transient Simulations of a T100 Micro Gas Turbine Converted Into a Micro Humid Air Turbine," ASME Paper No. GT2015-43277.
[27] Aurelia Turbine Website, 2023, "Aurelia Turbine Website," Aurelia Turbines Oy, Lappeenranta, Finland, accessed June 12, 2023, https://aureliaturbines.com/
[28] Capstone Turbine Website, 2023, "Capstone Turbine Website," Capstone Green Energy Corporation, Los Angeles, CA, accessed June 12, 2023, https://www.capstoneturbine.com/
[29] Flex Energy Solutions, 2023, "Flex Energy Website," Flex Energy Solutions, Portsmouth, NH, accessed June 12, 2023, https://www.flexenergy.com/
[30] MITIS Website, 2023, "Net Zero by 2050," MITIS SA, Liège, Belgium, accessed June 12, 2023, https://www.mitis.be/
[31] ODYSSEE-MURE, 2024, "Electricity Consumption per Dwelling | Electricity Dwelling | ODYSSEE-MURE," Odyssee-Mure Project, Brussels, Belgium, accessed Oct. 22, 2024, https://www.odyssee-mure.eu/publications/efficiency-by-sector/households/electricity-consumption-dwelling.html
[32] MTT Website, 2023, "MTT Micro Turbine Technology," Micro Turbine Technology BV, Eindhoven, Netherlands, accessed June 12, 2023, https://www.mtt-eu.com/
[33] Bladon Jets Website, 2023, "Bladon Jets Website," Bladon Micro Turbine, Coventry, UK, accessed June 12, 2023, https://www.bladonmt.com/
[34] Galanti, L., and Massardo, A., 2011, "Micro Gas Turbine Thermodynamic and Economic Analysis Up to 500 kWe Size," Appl. Energy, **88**(12), pp. 4795–4802.
[35] Jain, S., Roy, S., Aggarwal, A., Gupta, D., Kumar, V., and Kumar, N., 2015, "Study on the Parameters Influencing Efficiency of Micro-Gas Turbines: A Review," ASME Paper No. POWER2015-49417.
[36] Kim, M., Kim, J., and Kim, T., 2018, "The Effects of Internal Leakage on the Performance of a Micro Gas Turbine," Appl. Energy, **212**, pp. 175–184.
[37] Lee, Y.-B., Park, D.-J., Kim, C.-H., and Ryu, K., 2007, "Rotordynamic Characteristics of a Micro Turbo Generator Supported by Air Foil Bearings," J. Micromech. Microeng., **17**(2), pp. 297–303.
[38] Delanaye, M., Giraldo, A., Nacereddine, R., Rouabah, M., Fortunato, V., and Parente, A., 2017, "Development of a Recuperated Flameless Combustor for an Inverted Brayton Cycle Microturbine Used in Residential Micro-CHP," ASME Paper No. GT2017-65271.
[39] Fortunato, V., Henrara, E., Delanaye, M., and Parente, A., 2015, "An Optimization-Based Approach for the Development of a Combustion Chamber for Residential Micro-Gas Turbine Applications," Chem. Eng. Trans., **43**, pp. 2113–2118.
[40] McBride, B. J., Zehe, M. J., and Gordon, S., 2002, "NASA Glenn Coefficients for Calculating Thermodynamic Properties of Individual Species," Glenn Research Center, Cleveland, OH, pp. 1–295.
[41] Camporeale, S., and Fortunato, B., 2000, "Aero-Thermodynamic Simulation of a Double-Shaft Industrial Evaporative Gas Turbine," ASME Paper No. 2000-GT-0171.
[42] Battin-Leclerc, F., Blurock, E., Bounaceur, R., Fournet, R., Glaude, P.-A., Herbinet, O., Sirjean, B., and Warth, V., 2011, "Towards Cleaner Combustion Engines Through Groundbreaking Detailed Chemical Kinetic Models," Chem. Soc. Rev., **40**(9), pp. 4762–4807.
[43] Fortunato, V., Giraldo, A., Rouabah, M., Nacereddine, R., Delanaye, M., and Parente, A., 2018, "Experimental and Numerical Investigation of a MILD Combustion Chamber for Micro Gas Turbine Applications," Energies, **11**(12), p. 3363.
[44] De Paepe, W., Coppitters, D., Abraham, S., Tsirikoglou, P., Ghorbaniasl, G., and Contino, F., 2019, "Robust Operational Optimization of a Typical Micro Gas Turbine," Energy Proc., **158**, pp. 5795–5803.